Torque Estimation for Robotic Joint With Harmonic Reducer Based on Deformation Calibration

Yanshu Song, Hailin Huang, Fei Liu, Fengfeng(Jeff) Xi, Dunyi Zhou, and Bing Li

Abstract—**Joint torque sensing is an important technique for high-performance control of modern robotic systems, especially in an environment that requires man-machine collaboration. However, in many cases, traditional torque sensors are not suitable for robots because of the inevitable increase of joint flexibility and joint size. To address this problem, two novel methods are proposed to estimate torque of robotic joint with harmonic reducer via calibration of its existing flexibility without the need for any additional elastic elements. The first approach utilizes a new harmonic drive compliance model, which is more convenient for calibration and less dependent on the manufacturer's parameters to estimate the output torque. The second method relies on a system based on a back-propagation (BP) neural network to fit the non-linear relationship among the output torque, motor current, and other information that can be obtained from double encoders mounted on motor-side and load-side. The two proposed methods were experimentally investigated and the results show that the estimated torque values were in good agreement with the measurements obtained using a commercial torque sensor. Finally, different suitable application scenarios are presented according to the specific performance of each technique.**

Index Terms—**Torque estimation, robotic joint, harmonic drive compliance model, BP neural network.**

I. INTRODUCTION

TO improve the performance of high-speed, heavy-duty and high-precision robots, it is necessary to implement advanced control methods considering the dynamic model of the robots, such as moment control [1]–[3], and torque feedback control [4], [5]. In addition, it is often necessary for robots to cooperate with humans to perform specialized tasks, so compliance control of the manipulator is critical to ensure the safety of the operators [6]–[8]. These control methods are based on the complete dynamic model of the robots, and one of the most important factors in determining the control effect is the accurate and real-time measurement of the output torque of the robotic joints.

The most common way to measure the joint output torque is to install a multi-axis torque sensor at the end of the robot [9] to facilitate the calculation of the output torque of each joint, via a transformation based on the Jacobian matrix

Yanshu Song, Hailin Huang, Fei Liu, Fengfeng(Jeff) Xi, Dunyi Zhou, and Bing Li are with Harbin Institute of Technology, Shenzhen, 518055, China (e-mail: songyanshu@stu.hit.edu.cn; huanghailin@hit.edu.cn; liufei@stu.hit.edu.cn; fengxi@ryerson.ca; zhoudunyi@stu.hit.edu.cn; libing.sgs@hit.edu.cn). Fengfeng(Jeff) Xi is also with the Department of Aerospace Engineering Ryerson University, Toronto, Canada.

[10]. However, due to the complexity of the calculations, the measurement results are typically delayed and large errors are inevitable [11]–[13]. Another common measurement scheme involves the installation of a torque sensor based on an elastic element [14] at the output side of each joint. This method can effectively reduce computational complexity and improve real-time performance, but it also dramatically increases cost. Numerous other measurement methods have been proposed in recent years. Sarmad [15], [16] proposed a compact and lightweight design for a torque sensor based on an optical technique to detect angular displacement in joints. Kawakami [17] used a linear encoder to measure the torsional deformation of an additional elastic body. However, there is a common drawback in these measurement methods in that the installation of an additional elastic element in the joint inevitably increases joint flexibility and thus affects the accuracy of position control. Moreover, the addition of an elastic element also increases the size of the robotic joint, which limits their applicability in some narrow space situations.

For robotic joints equipped with harmonic reducers, built-in torque sensing is a widely investigated techniques. Researchers [18], [19] have proposed different methods for attaching strain gauges to the flex-spline of harmonic reducers to measure their deformation for subsequent use to calculate the output torque. This avoids the increase of joint flexibility or changes to their mechanical structure. However, an inherent drawback of the built-in torque method is that relatively large torque ripples are generated due to the elliptical shape of the harmonic flex-spline, gear meshing vibration, and position measurement inaccuracy of the strain gauges [20]. Kim [21], [22] proposed a simple and effective method to compensate for fluctuations of the electrical signal by changing the installation position of Wheatstone bridges. Jung and Byungjin [23], [24] proposed an algorithmic compensation for torque ripples and effectively addressed the lack of order information at low velocities, using a back-propagation method that incorporated trained order sampling data. However, because of the need to position and orient cement strain gauges precisely, the aforementioned methods all require a secondary assembly of the harmonic reducers inside the robotic joint, which inevitably affects its accuracy and may even cause irreparable damage. As such, these approaches cannot be widely used.

In recent years, the use of high-precision, and high-resolution magnetic grid encoders [25], [26] with a small size and low cost have increased. These devices facilitate the measurement of torsional deformation of harmonic reducers using double encoders (installed at the motor-side and the output-side respectively). Zhang [27], [28] proposed several methods

for the estimation of the output torque by solving the harmonic drive compliance model using the total torsional angle of the harmonic reducer measured via the double encoders. This avoids the inherent drawbacks in the built-in torque sensing methods. Shi [29], [30] modified the low-pass filter in [28] and demonstrated that their proposed algorithm can optimally and robustly adapt torque estimation filtering to load variations by self-tuning the filtering gain and self-switching the filtering modes between optimal and robust. However, these methods require manufacturers to provide accurate calibration parameters and current information of the driving motor, which are difficult to obtain in some situations. Moreover, the calibration process is complex and computationally intensive.

In this paper, two novel methods for estimating the output torque of a robotic joint with a harmonic reducer are proposed, based on modeling and a BP neural network. In the first method, we utilize the idea of distortion of harmonic reducer decomposition in [27] and improve the fitting models of each component such that the new model no longer requires the accurate calibration parameters provided by the manufacturers. Moreover, the final calibration process is simplified and less computationally intensive, which could potentially improve the application prospects and service performances of robotic joint torque estimation methods based on deformation modeling. In the second method, the BP neural network is first trained using several sets of sample data obtained via experiments. The well-trained network system is then able to fit the non-linear relationship that exists among the joint output torque, total torsional angle of the harmonic reducer, current of the driving motor, and some other measurable information. Subsequently, the joint output torque can be estimated by inputting this corresponding measurable information into the well-trained neural network system.

The remainder of this paper is organized into several sections. The specific principles and implementation processes of the two proposed methods (based on modeling and the BP neural network) are presented in Section II and Section III, respectively. A brief introduction of the experimental setup and the analysis of the experiment results are presented in Section IV. Finally, the main conclusions and remarks are summarized in Section V.

II. METHOD BASED ON IMPROVED DEFORMATION MODELING

As shown in Fig. 1, the harmonic reducer has three basic components, including a wave generator, a flex-spline, and a circular spline. The wave generator is the input torque interface and consists of two independent parts: an external ball bearing and an elliptical wave generator plug that is inserted into the bearing to make it elliptical. The flex-spline clings tightly to the ball bearing, and it deforms into an elliptical shape without relative sliding to the outer ring of the ball bearing when the plug rotates. The inner ring of the circular spline and the outer ring of the flex-spline are connected by splines with different numbers of teeth. When the flex-spline is elliptically deformed by the wave generator, it moves relative to the circular spline, and the ratio of its speed to the rotating speed of the wave
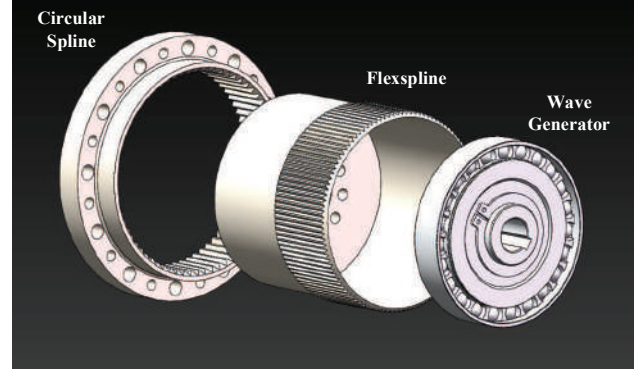

Fig. 1. Decomposition structure diagram of harmonic reducer.

generator is determined by the difference in the number of teeth.

A. Basic Composition of Harmonic Reducer Deformation

When a harmonic reducer is installed in a robotic joint, the circular spline is generally fixed on the base. The wave generator and flex-spline are usually used as the input and output, respectively, and the ideal angular position relationship between them is as follows:

$$\theta_i = N\theta_o \tag{1}$$

where θ_i is the input side angular position, θ_0 is the output side angular position, and N is the reduction ratio. Equation (1) denotes the ideal relationship between the absolute angular positions of the input and output side of the harmonic reducer where it is regarded as a fully rigid gear reducer. However, this relationship is non-linear for an actual harmonic reducer, according to the measurement results in reference [31], which means that there is an angle difference caused by deformation. The torsional angle of a typical harmonic reducer varies with the external load as shown in Fig. 2. It can be seen that the relationship has strong nonlinearity and hysteresis (B to B'). When the external torque load increases or decreases from different positions (A, I_1, I_2, D_1, D_2, A'), the curve changes irregularly as the black solid and dotted lines. Therefore, it is difficult to characterize this relationship using the traditional non-linear curve calibration methods.

This complex and irregular non-linear relationship is caused by the torsional flexibility of the harmonic drive components, the non-linear viscous friction, and the kinematic error caused by gear meshing. Fig. 3 is the key angular position of the harmonic drive, and it can be seen that the total harmonic deformation consists of three parts: wave generator deformation, flex-spline deformation, and kinematic error.

The kinematic error θ_{err} indicates the angular difference between the output side of the wave generator and the input side of the flex-spline. This error is caused by machining and assembly inaccuracies of the gears [32]. It can be defined as follows:

$$\theta_{err} = \theta_{fsi} - \frac{\theta_{\omega go}}{N} \tag{2}$$
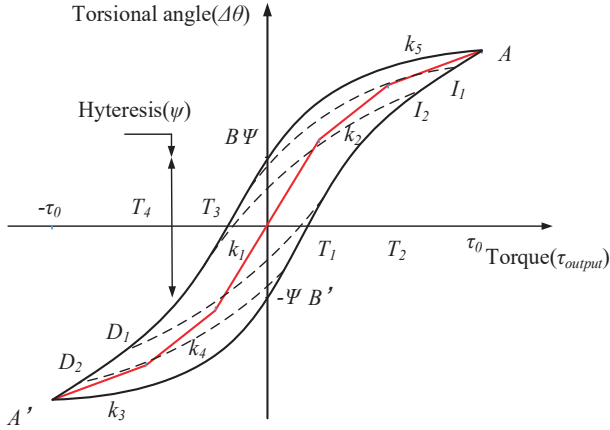
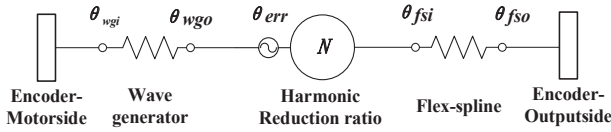Fig. 2. The relationship between the total torsional angle of the harmonic reducer and its output torque.

Fig. 3. Key angular position in harmonic drive.

The flex-spline torsional angle $\Delta\theta_f$ represents the deformation of the flex-spline when subjected to an external load, which can be defined as follows:

$$\Delta\theta_f = \theta_{fso} - \theta_{fsi} \tag{3}$$

Similarly, the wave generator torsional angle $\Delta\theta_\omega$ represents the total deformation of the elastic damper elements in wave generator under the input of a motor torque. It can be defined as follows:

$$\Delta\theta_\omega = \theta_{\omega go} - \theta_{\omega gi} \tag{4}$$

Among them, θ_{fsi} and θ_{fso} represent the absolute angular positions of the input-side and output-side of the flex-spline. $\theta_{\omega go}$ and $\theta_{\omega gi}$ represent the absolute angular positions of the motor-side (wave generator plug) and the output-side (outer edge of ball bearing) of the wave generator. Given that $\theta_{\omega gi}$ and θ_{fso} represent the input-side and the output-side of the harmonic drive, respectively, the total torsional angle of the harmonic reducer can be expressed as follows:

$$\Delta\theta = \theta_{fso} - \frac{\theta_{\omega gi}}{N} \tag{5}$$

where N is the reduction ratio of harmonic reducer. Substituting (2), (3) and (4) into (5) yields:

$$\Delta\theta = \Delta\theta_f + \frac{\Delta\theta_\omega}{N} + \theta_{err} \tag{6}$$

B. Improved Fitting Model for Each Basic Deformation Part

(1) Deformation of the flex-spline: According to the experiments of the harmonic reducer manufacturer [33], the total deformation of a harmonic drive is mainly caused by

the flexibility of the flex-spline and its torsional angle is piecewise linearly related to the output torque. We divided the output torque within the rated torque range into five segments and designed the following piecewise linear functions, whose curves are represented by the red line in Fig. 2.

$$\Delta\theta_f = \begin{cases} -k_1\frac{\tau_0}{3} - k_2\frac{\tau_0}{3} + k_3(T_f + \frac{2\tau_0}{3}) & T_f \in [-a \ -b) \\ -k_1\frac{\tau_0}{3} + k_2(T_f + \frac{\tau_0}{3}) & T_f \in [-b \ -c) \\ k_1 T_f & T_f \in [-c \ c) \\ k_1\frac{\tau_0}{3} + k_4(T_f - \frac{\tau_0}{3}) & T_f \in [c \ b) \\ k_1\frac{\tau_0}{3} + k_4\frac{\tau_0}{3} + k_5(T_f - \frac{2}{3}\tau_0) & T_f \in [b \ a] \end{cases} \tag{7}$$

Among them, k_1, k_2, k_3, k_4 and k_5 represent the reciprocal of the stiffness coefficients of the flex-spline for different output torque ranges. a, b and c are equal to τ_0, $\frac{2\tau_0}{3}$, $\frac{\tau_0}{3}$, respectively.

(2) Deformation of the wave generator: The hysteresis of the harmonic drive is mainly caused by the compliance and friction in the wave generator. It can be seen from Fig. 2 that the harmonic output torque is constant to 0 when the input torque of the wave generator is within the starting torque range($-\Psi$ to Ψ). According to the experiments of [28], the torsional angle of the wave generator has a definite non-linear relationship with the input torque that originates from the connected DC motor. In addition, the motor current is directly measurable through the motor driver, and can be used to represent the input torque, as there is a definite linear relationship between them. The following six-order polynomial was designed to fit the relationship between the torsional angle of the wave generator and the motor current.

$$\Delta\theta_{\omega g} = \omega_0 + \omega_1 I + \omega_2 I^2 + \omega_3 I^3 + \omega_4 I^4 + \omega_5 I^5 + \omega_6 I^6 \tag{8}$$

(3) Kinematic error: The kinematic error is caused by the micro-backlash and deformation in the splines of the flex-spline and the circular spline. Its magnitude is related to the machining accuracy of the gear profile and the overall assembly accuracy of the harmonic reducer. The experiments in [34] show that the kinematic error of a certain harmonic reducer varies periodically with the absolute angular position and the absolute angular velocity of its input and output side. The finite Fourier series is a simple and precise mathematical tool for appropriating periodically varying signals. We design the following function to fit the relationship among the kinematic error, the angular position and the angular velocity of the harmonic reducer.

$$\theta_{err} = a_0 + \sum_{n=1}^{3} [a_n \cos(n\theta_{fso}\omega_{fso}) + b_n \sin(n\theta_{fso}\omega_{fso}) + c_n \cos(n\theta_{\omega gi}\omega_{\omega gi}) + d_n \sin(n\theta_{\omega gi}\omega_{\omega gi})] \tag{9}$$

C. Calibration of Fitting Model Coefficients

(1) Model coefficients calibration equation: According to the formula (6), the total deformation of the harmonic reducer consists of flex-spline deformation, wave generator deformation,

and kinematic error. By introducing (7), (8) and (9) into (6), a piecewise linear equation of the coefficients to be calibrated is obtained as follows:

$$\Delta\theta = \begin{cases} h - \frac{\tau_0}{3}k_1 - \frac{\tau_0}{3}k_2 + (T_f + \frac{2\tau_0}{3})k_3 & T_f \in [-a \ -b) \\ h - \frac{\tau_0}{3}k_1 + (T_f + \frac{\tau_0}{3})k_2 & T_f \in [-b \ -c) \\ h + T_f k_1 & T_f \in [-c \ c) \\ h + \frac{\tau_0}{3}k_1 + (T_f - \frac{\tau_0}{3})k_4 & T_f \in [c \ b) \\ h + \frac{\tau_0}{3}k_1 + \frac{\tau_0}{3}k_4 + (T_f - \frac{2}{3}\tau_0)k_5 & T_f \in [b \ a] \end{cases}$$
(10)

where a, b, and c are equal to τ_0, $\frac{2\tau_0}{3}$, $\frac{\tau_0}{3}$, respectively, and

$$h = \sum_{n=1}^{3} [a_n \cos(n\theta_{fso}\omega_{fso}) + b_n \sin(n\theta_{fso}\omega_{fso}) +$$

$$c_n \cos(n\theta_{wgi}\omega_{wgi}) + d_n \sin(n\theta_{wgi}\omega_{wgi})] + k_0 + \frac{1}{N}\sum_{i=1}^{6} I^i \omega_i$$

$$k_0 = \frac{\omega_0}{N} + a_0$$

(2) Acquisition of required variables: θ_{wgi} and θ_{fso} can be measured by high precision magnetic grid encoders installed on the motor-side and the load-side of the harmonic reducer, respectively, as follows:

$$\theta_{wgi} = \frac{\theta_{MEncoder} - \theta_{MEncoderinit}}{R_M} \times 360 \quad (11)$$

$$\theta_{fso} = \frac{\theta_{LEncoder} - \theta_{LEncoderinit}}{R_L} \times 360 \quad (12)$$

where $\theta_{MEncoder}$, $\theta_{MEncoderinit}$ and R_M are the current value, initial value, and the resolution of the motor-side encoder, respectively. Similarly, $\theta_{LEncoder}$, $\theta_{LEncoderinit}$, and R_L represent these values on the load-side encoder.

ω_{wgi} and ω_{fso} represent the absolute angular velocity of the motor-side and the load-side of the harmonic reducer, respectively. They can be obtained from the angular positions as follows:

$$\omega_{wgi} = \frac{\theta_{wgicurrent} - \theta_{wgilast}}{\Delta t} \quad (13)$$

$$\omega_{fso} = \frac{\theta_{fsocurrent} - \theta_{fsolast}}{\Delta t} \quad (14)$$

where Δt represents the sampling interval.

In addition, $\Delta\theta$ can be calculated by substituting (11) and (12) into (5). T_f and I can be measured directly using a commercial torque sensor and motor driver, respectively.

(3) Optimizing method for coefficients solution: The piecewise linear equation of model coefficients (10) within each subinterval can be simplified to the following matrix form:

$$Ax = b \quad (15)$$

where $A \in R^{m*n}$, $b \in R^m$ and vector x consists of all coefficients in the calibration model. Matrix A and vector b are formed using a large amount of data measured in the experiments and they satisfy the following: $m \geq n$, and $rank(A) = n$. In this case, the number of unknown variables

is less than the number of equations, so the equations probably do not have an effective solution. We propose to calculate the optimum solution and to construct an objective function of global error as follows:

$$\begin{aligned} f(x) &= \|Ax - b\|^2 \\ &= (Ax - b)^T(Ax - b) \\ &= \frac{1}{2}x^T\left(2A^TA\right)x - x^T\left(2A^Tb\right) + b^Tb \end{aligned}$$
(16)

Clearly, $f(x)$ is a quadratic function and given that $rank(A) = n$, its quadratic form is positive definite. According to the first-order necessary conditions of local minima, the minimum should satisfy the following:

$$\nabla f(x) = 2A^TAx - 2A^Tb = 0 \quad (17)$$

Therefore, the optimum solution can be directly calculated using the following formula:

$$x^* = \left(A^TA\right)^{-1}A^Tb \quad (18)$$

where, for all $x \in R^n$, the following formula is valid:

$$\|Ax - b\|^2 \geq \|Ax^* - b\|^2$$

Sample data is generated continuously in the experimental process; therefore, there exists a problem of model updating. The result of the preceding formula can be used as the original solution:

$$x_0 = G_0^{-1}A_0^Tb^0 \quad (19)$$

where $G_0 = A_0^TA_0$. When the new samples A_1 and b_1 are introduced, the challenge is to minimize the value of the following formula:

$$\left\| \begin{bmatrix} A_0 \\ A_1 \end{bmatrix} x - \begin{bmatrix} b_0 \\ b_1 \end{bmatrix} \right\|^2$$

Similarly, according to the first-order necessary conditions of the local minima, the solution of the preceding equation is:

$$x^1 = G_1^{-1} \begin{bmatrix} A_0 \\ A_1 \end{bmatrix}^T \begin{bmatrix} b_0 \\ b_1 \end{bmatrix} \quad (20)$$

where G_1 is:

$$G_1 = \begin{bmatrix} A_0 \\ A_1 \end{bmatrix}^T \begin{bmatrix} A_0 \\ A_1 \end{bmatrix}$$

Then we can obtain the iterative equations [35]:

$$G_{k+1} = G_k + A_{k+1}^T A_{k+1} \quad (21)$$

$$x^{k+1} = x^k + G_{k+1}^{-1}A_{k+1}^T\left(b_{k+1} - A_{x+1}x^k\right) \quad (22)$$

According to the preceding formulas, it is necessary to determine the inverse of the matrix G_k. Given that the process of finding the inverse of a matrix is a computationally resource-consuming task, a transformation is required to simplify this process. It can be determined that the inverse of the matrix in

the previous step is related to the inverse of the matrix in the current step in an iteration process. Therefore, we have:

$$P_k = G_k^{-1}$$

Then the iterative formulas can be modified as follows, according to the Sherman-Morrison-Woodbury (SMW) formula [36]:

$$
\begin{aligned}
P_{k+1} &= P_k - P_k A_{k+1}^T \left(I + A_{k+1} P_k A_{k+1}^T \right)^{-1} A_{k+1} P_k \\
&= P_k - P_k A_{k+1}^T \left(I - \frac{A_{k+1} P_k A_{k+1}^T}{1 + A_{k+1}^T A_{k+1} P_k} \right) A_{k+1} P_k
\end{aligned}
\tag{23}
$$

$$x^{k+1} = x^k + P_{k+1} A_{k+1}^T \left(b_{k+1} - A_{k+1} x^k \right) \tag{24}$$

In particular, when there is only one row in the new sample, the formulas can be further simplified as follows:

$$P_{k+1} = P_k - \frac{P_k \alpha_{k+1} \alpha_{k+1}^T P_k}{1 + \alpha_{k+1}^T P \alpha_{k+1}} \tag{25}$$

$$x^{k+1} = x^k + P_{k+1} \alpha_{k+1}^T \left(b_{k+1} - \alpha_{k+1} x^k \right) \tag{26}$$

where:

$$\alpha_{k+1}^T = A_{k+1}$$

According to the preceding principles, the deformation model coefficients can be calibrated using the experimentally obtained data, and the fitting model coefficients of the wave generator component (8) and kinematic error component (9) are summarized in Table I.

The fitting model coefficients of the flex-spline are as follows:

$$
\begin{bmatrix} k_1 \\ k_2 \\ k_3 \\ k_4 \\ k_5 \end{bmatrix}
=
\begin{bmatrix} 0.26305 \\ 0.19913 \\ 0.04946 \\ 0.29008 \\ 0.08434 \end{bmatrix}
$$

D. Torque Estimation

The relationship among the output torque of the harmonic reducer, motor current, absolute angular position, and angular velocity in the motor-side and load-side is established in the aforementioned modeling process. The optimum solutions of all the fitting model coefficients are obtained in the calibration process. Finally, the process of using this measurable information to calculate the output torque of the robotic joint with a harmonic reducer can be divided into two steps. The first step is to determine the torsional angle of flex-spline, given that there is a piecewise linear relationship between this parameter and the output torque. The equation is as follows:

$$
\begin{aligned}
\Delta \theta_f = &- \sum_{n=1}^{3} [a_n \cos(n\theta_{fso}\omega_{fso}) + b_n \sin(n\theta_{fso}\omega_{fso}) + \\
& c_n \cos(n\theta_{wgi}\omega_{wgi}) + d_n \sin(n\theta_{wgi}\omega_{wgi})] + \\
& \Delta \theta - k_0 - \frac{1}{N} \sum_{i=1}^{6} I^i \omega_i
\end{aligned}
\tag{27}
$$

Then the joint output torque estimation value can be obtained using the inverse of (7).

$$
T_f =
\begin{cases}
(\Delta\theta_f + k_1 \frac{\tau_0}{3} + k_2 \frac{\tau_0}{3})/k_3 - \frac{2\tau_0}{3} & \Delta\theta_f \in [a \quad b) \\
(\Delta\theta_f + k_1 \frac{\tau_0}{3})/k_2 - \frac{\tau_0}{3} & \Delta\theta_f \in [b \quad c) \\
\Delta\theta_f / k_1 & \Delta\theta_f \in [c \quad d) \\
(\Delta\theta_f - k_1 \frac{\tau_0}{3})/k_4 + \frac{\tau_0}{3} & \Delta\theta_f \in [d \quad e) \\
(\Delta\theta_f - k_1 \frac{\tau_0}{3} - k_4 \frac{\tau_0}{3})/k_5 + \frac{2}{3}\tau_0 & \Delta\theta_f \in [e \quad f]
\end{cases}
\tag{28}
$$

where a, b, c, d, e and f equal to $-\tau_0, -\frac{1}{3}\tau_0 (k_1 + k_2)$, $-\frac{1}{3}\tau_0 k_1, \frac{1}{3}\tau_0 k_1, \frac{1}{3}\tau_0 (k_1 + k_4)$, respectively.

III. METHOD BASED ON BP NEURAL NETWORK

The neural network algorithms simulate the network structure of the local adjustment and mutual coverage of the acceptance domain in the human brain. The BP neural network is the most widely used and efficient model to appropriate continuous non-linear relationships with strong non-linear mapping ability and flexible network structure. The numbers of hidden layers and neurons in each layer can be set arbitrarily according to the specific usage requirements. As the number of layers and neurons increases, the fitting accuracy improves. However, the calculation time also increases. The BP neural network is a global approximation network and all the weights are re-adjusted when learning a new sample, which makes it suitable for fitting relationships with strong non-linearity. We propose to build a fitting system based on the BP neural network, to approximate the non-linear relationship among the output torques of the harmonic reducer and the measurable input variables previously mentioned, and then to train it using sample data obtained from experiments under various special conditions. Finally, the output torque can be estimated by the well-trained network system and the corresponding input variables.

A. Selection and Pretreatment of Input Vector Elements

It is evident from the preceding discussion that the deformation of the wave generator is determined by the motor torque (τ_{motor}) and the kinematic error is determined by the absolute angular positions (θ_{wgi} and θ_{fso}) and angular velocities (ω_{wgi} and ω_{fso}) of the harmonic input-side and output-side. The output torque of the harmonic reducer has a piecewise linear relationship with the torsional angle of the flex-spline, which can be calculated by subtracting the deformation of the wave generator and kinematic error from the total torsional angle ($\Delta\theta$). Therefore, the harmonic output torque has a definite

TABLE I
FITTING MODEL COEFFICIENTS OF WAVE GENERATOR COMPONENT AND KINEMATIC ERROR COMPONENT

T_f range	$\left[-\tau_0 - \frac{2}{3}\tau_0\right)$	$\left[-\frac{2}{3}\tau_0 - \frac{1}{3}\tau_0\right)$	$\left[-\frac{1}{3}\tau_0 \frac{1}{3}\tau_0\right)$	$\left[\frac{1}{3}\tau_0 \frac{2}{3}\tau_0\right)$	$\left[\frac{2}{3}\tau_0 \tau_0\right]$
w_1	-388.278	-2804.237	-6044.592	-68.281	-5449.492
w_2	-749.239	5204.185	4119.795	463.950	-13993.609
w_3	1016.636	3740.866	5439.054	-3366.580	104057.327
w_4	1982.376	-6419.311	-6014.647	-746.738	-151456.711
w_5	991.0376	-5631.224	-2381.304	5430.041	80741.904
w_6	158.3482	-927.7504	2287.355	-2449.350	-14277.104
a_1	-0.0568	0.0696	2.080	-0.0245	0.1833
a_2	-0.1012	0.5732	-2.586	0.0309	-0.1646
a_3	0.01283	-0.0612	1.7197	0.3531	-0.1588
b_1	0.14811	-0.0970	-0.220	-0.1507	0.0463
b_2	0.07148	-0.1757	-0.0064	0.2039	-0.0741
b_3	0.02537	-0.0106	0.2450	-0.0027	0.1218
c_1	0.0515	-0.1775	1.996	0.0113	-0.0501
c_2	-0.0480	0.0608	0.196	0.1082	-0.0618
c_3	-0.0282	-0.1716	1.818	-0.2669	0.00287
d_1	0.0961	-0.1285	0.166	0.0795	-0.0871
d_2	-0.0480	0.0608	0.196	0.1082	-0.0618
d_3	0.0818	-0.0286	0.132	0.0507	-0.0401
k_0^T	38.2570	15.3286	4.7329	5.2152	-8.7800

non-linear relationship with these six kinds of measurable information, which can be expressed as follows:

$$T_f = f(\tau_{motor}, \theta_{wgi}, \theta_{fso}, \omega_{wgi}, \omega_{fso}, \Delta\theta) \quad (29)$$

We choose the motor current to replace the motor output torque because it can be measured directly by the motor driver. As such, it can be concluded that the input vector of the neural network system is as follows:

$$Input = [I, \theta_{wgi}, \theta_{fso}, \omega_{wgi}, \omega_{fso}, \Delta\theta]$$

The feedback of the original current signal is unstable with a large fluctuation amplitude and stochastic noise because of the joint friction, damping, and the delay of the motor driver. The BP neural network is better at fitting stable and slow fluctuating signals; therefore, its robustness and accuracy will be influenced if the original signal is directly used as an element in the input vector. The Kalman filter is an effective method for reducing the impact of noise and for efficiently separating the required variable from the observed signal. We propose to use this algorithm to adjust and correct the current signal.

The state equation and observation equation of a linear system to be measured can be expressed as (30) and (31), respectively:

$$X(k) = FX(k-1) + BW(k-1) \quad (30)$$
$$Z(k) = HX(k) + V(k) \quad (31)$$

$X(k)$ and $X(k-1)$ are the estimated values at time k and time k-1, respectively. $Z(k)$ is the measurement value from the motor driver at time k. W and V represent the stochastic noise of the control process and measurement process, respectively. F, B, H are determined by the properties of the observed linear system and the measurement system.

In this paper, the Kalman filter is used to correct the current data, which is a one-dimensional variable, so F, H and B should be taken as 1. The feedback period of the original current data is 0.5 ms and the Kalman filter is applied to process the original data at every 20 ms interval. The speed of the motor is slow when subjected to external loads, so the motor current change is not obvious during the estimation period and the variance of the noise W can be taken as 0.05 (Q). Similarly, the variance of the measurement noise V is 0.25 (R) according to the motor driver manual, and the initial value of the covariance P can be taken as 0.01.

The Kalman filter represents the variable to be estimated at time t using the belief $bel(x_t)$ based on the mean μ_t and the covariance Σ_t. The input is its belief at time $t-1$, represented by μ_{t-1} and Σ_{t-1}. The Kalman filter uses the control vector μ_t and the measurement vector z_t to update these parameters and the output is the belief of the variable at time t, represented by μ_t and Σ_t. The implementation process of the Kalman filter algorithm is as follows [37]:

$$\overline{\mu}_t = A_t\mu_{t-1} + B_t u_t \quad (32)$$
$$\overline{\Sigma}_t = A_t\Sigma_{t-1}A_t^T + R_t \quad (33)$$
$$K_t = \overline{\Sigma}_t C_t^T \left(C_t\overline{\Sigma}_t C_t^T + Q_t\right)^{-1} \quad (34)$$
$$\mu_t = \overline{\mu}_t + K_t\left(z_t - C_t\overline{\mu}_t\right) \quad (35)$$
$$\Sigma_t = \left(I - K_t C_t\right)\overline{\Sigma}_t \quad (36)$$

Based on this principle, we designed a filtering program for the original current data and the flow chart of the algorithm is
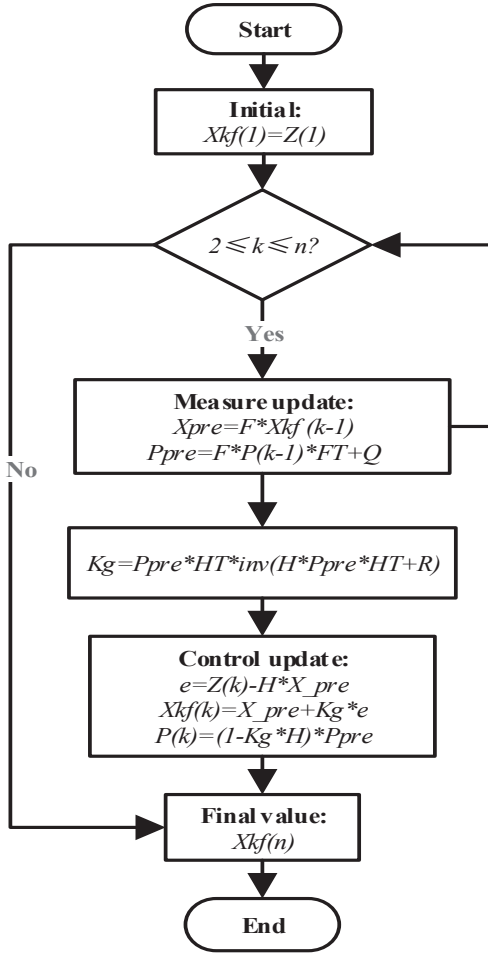
Fig. 4. Flow chart of motor current filtering algorithm.

Fig. 5. Comparison of current data before and after filtering.

shown in Fig. 4. A comparison of the current data before and after filtering is shown in Fig. 5. It is evident that the filter algorithm can reduce the fluctuation amplitude of the signal by half, thereby making it smoother.

B. Fitting System Based on BP neural network

The core idea of the BP neural network is to adjust the weight neurons in each layer to minimize the difference between the final network output and expected output [38]. The schematic diagram of the fitting system based on the BP neural network is shown in Fig. 6. The input layer, the hidden layer, and the output layer of this system have n, p, and q neurons, respectively, and the variables are as follows:

Input vector: $x = (x_1, x_2, \cdots, x_n)$

Hidden layer input vector: $hi = (hi_1, hi_2, \cdots, hi_q)$

Hidden layer output vector: $ho = (ho_1, ho_2, \cdots, ho_p)$

Output layer input vector: $yi = (yi_1, yi_2, \cdots, yi_q)$

Output layer output vector: $yo = (yo_1, yo_2, \cdots, yo_q)$

Expected output vector: $d = (d_1, d_2, \cdots, d_q)$

Connection weights between input layer and middle layer: w_{ih}

Connection weights between hidden layer and output layer: w_{ho}

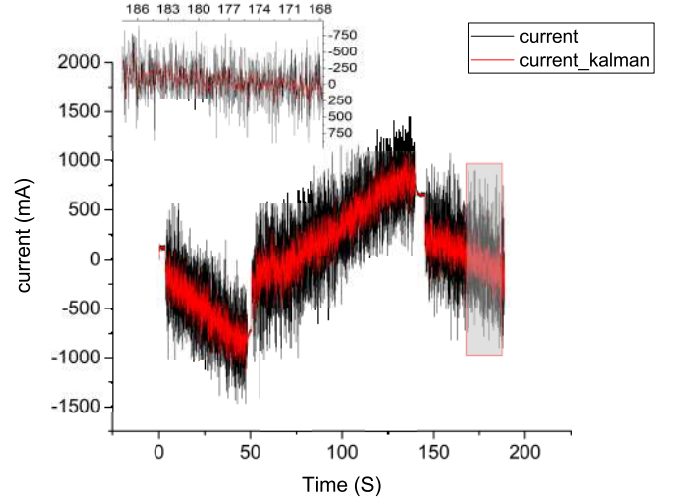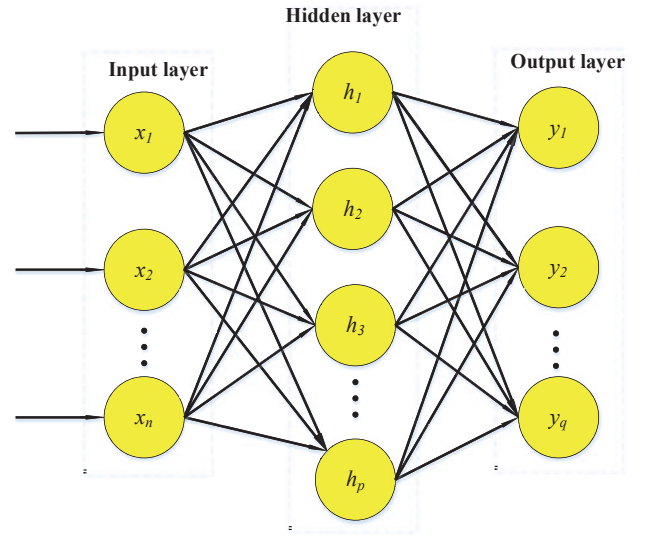Threshold of neurons in the hidden layer: b_h

Fig. 6. A schematic diagram of the fitting system based on the BP neural network.

Threshold of neurons in the output layer: b_o

Sample data number: $k = 1, 2 \cdots m$

Activation function: $f(x) = 1/(1 + e^{-x})$

Error function: $e = \frac{1}{2} \sum_{o=1}^{q} [d_o(k) - yo_o(k)]^2$

The training process can be divided into two alternately iterative processes: forward- and backward-propagation. The former involves inputting a training set that includes the input vector X and the expected output vector D to the current BP model via the input layer, the hidden layer, and output layer. The specific error for each input vector can then be obtained. In the BP process, the error is reversed and the weight of the neurons in each layer is updated until the output error is reduced to an acceptable level, or the number of learnings reaches the preset. The specific steps involved are as follows:

The first step is to initialize the connection weights of each layer to that of a random number in the interval (-1,1) and to set the acceptable error value E and the maximum number of learnings M, then to randomly select the kth input sample

$x(k)$ and the corresponding expected output $d(k)$.

$$x(k) = (x_1(k), x_2(k), \cdots, x_n(k)) \tag{37}$$
$$d(k) = (d_1(k), d_2(k), \cdots, d_q(k)) \tag{38}$$

The second step is to calculate the input and output of each neuron in the hidden layers and the output layers, as follows:

$$hi_i(k) = \sum_{i-1}^{n} w_{ih} x_i(k) - b_h, h = 1, 2, \cdots, p \tag{39}$$
$$ho_h(k) = f(hi_i(k)), h = 1, 2, \cdots, p \tag{40}$$
$$yi_o(k) = \sum_{h=1}^{p} w_{ho} ho_h(k) - b_o, o = 1, 2, \cdots, q \tag{41}$$
$$yo_o(k) = f(yi_o(k)), o = 1, 2, \cdots, q \tag{42}$$

Then the global error for this input sample can be obtained, as follows:

$$E = \frac{1}{2m} \sum_{k=1}^{m} \sum_{o=1}^{q} [d_o(k) - yo_o(k)]^2 \tag{43}$$

In the third step, the partial derivative of the global error to the output vector of the output layer is calculated and then retransmitted to the input layer via the hidden layer, using the derivative rule of the compound function. Finally, the corrected values of the connection weights in each layer are obtained according to the gradient descent method [39].

$$\Delta w_{ho}(k) = -\mu \frac{\partial e}{\partial w_{he}} = \mu \delta_h(k) ho_h(k) \tag{44}$$
$$\Delta w_{ih}(k) = -\mu \frac{\partial e}{\partial w_{ih}} = -\mu \frac{\partial e}{\partial hi_h(k)} \frac{\partial hi_h(k)}{\partial w_{ih}} = \delta_h(k) x_i(k) \tag{45}$$

where

$$\delta_h(k) = \left(\sum_{h=1}^{p} \delta_o(k) w_{ho} \right) f'(hi_h(k))$$
$$\delta_o(k) = (d_o(k) - yo_o(k)) f'(yi_o(k))$$

The connection weights are optimized via the following iteration:

$$w_{ho}^{N+1} = w_{ho}^{N} + \mu \Delta w_{ho}(k) \tag{46}$$
$$w_{ih}^{N+1} = w_{ih}^{N} + \eta \Delta w_{ih}(k) \tag{47}$$

The μ and η represent the learning rates that are used to adjust the step size to prevent divergence of the numerical solution.

The last step is to judge whether the global error meets the accuracy requirements, or the learning time is greater than the maximum value. The algorithm is terminated if one of these two conditions holds. Otherwise, it will select the next learning sample randomly and return to the second step to enter the next round of learning.

In the specific training process, we use a large amount of sample data obtained via experiments, especially, in special cases such as a sudden load change. The process is stopped
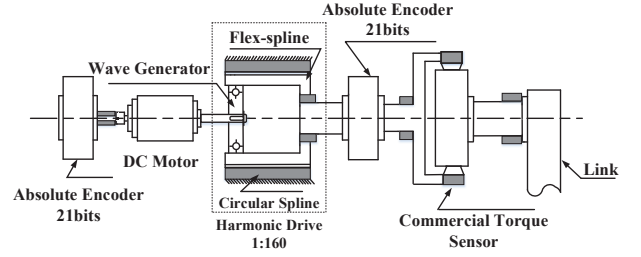

Fig. 7. Schematic diagram of experimental platform.

when the output error achieves the accuracy requirements. Finally, by inputting the corresponding measurable information of the motor current, the absolute angular position and the angular velocity of the joint's input-side and output-side into the well-trained neural network system, the estimation value of the output torque can be obtained.

IV. EXPERIMENT

A. Experimental Setup

To investigate the proposed torque estimation methods, we built an experimental platform and its schematic diagram is as shown in Fig. 7. It is evident that the wave generator is driven by a DC motor and the circular spline is fixed on the base, while the flex-spline acts as the output-side of the harmonic reducer whose reduction ratio and rated torque are 160:1 and 400 Nm, respectively. There are two 21-bit high-precision magnetic grid encoders installed at the motor-side and the output-side of the reducer, respectively. A commercial torque sensor is installed between the output-side of the harmonic reducer and the link to measure the actual output torque. Fig. 8 represents the experimental platform, where the end of the link is connected with weights by nylon rope to provide various loads.

B. Experimental Process and Results

The effectiveness of proposed torque estimation methods is verified by comparing the estimated torque values to the measurements obtained with a commercial torque sensor. Four experiments were designed including slow, fast, sudden loading, and the static step-by-step loading process.

The slow change of the load torque is achieved by controlling the joint to facilitate movement in a sinusoidal trajectory, because the weights connected at the end of the link gradually introduce a change in the load torque under different lengths of the force arms. For fast changing load torque process, this is achieved via irregular manual exertion of an external force at the link end in both directions. The sudden change of the load torque is realized by the sudden removal of all weights, i.e. the nylon rope suspended weights is cut off rapidly at a certain moment. Similarly, the static loading experiment was achieved by controlling the link to move to the horizontal position first, and then to move the nylon rope systematically from inside to outside.

In these four experiments, a comparison of the experimental results using the proposed method of torque estimation based
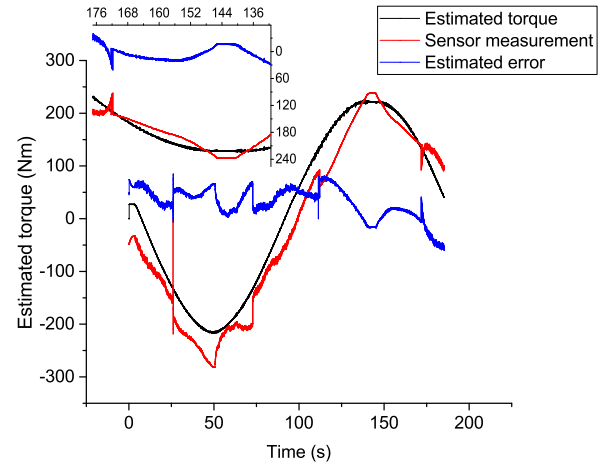
Fig. 8. Experimental setup.

Fig. 9. Estimated torque based on modeling versus the torque measured using a commercial torque sensor (slow load change).
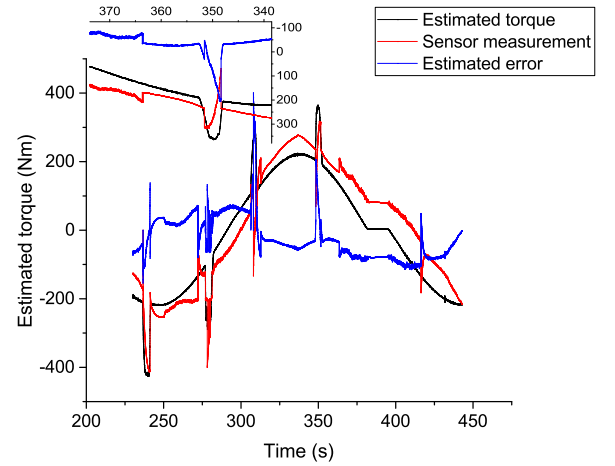

Fig. 10. Estimated torque based on modeling versus the torque measured using a commercial torque sensor (fast load change).
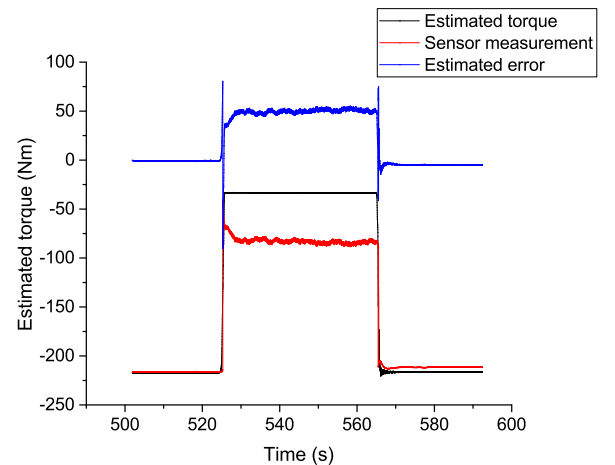

Fig. 11. Estimated torque based on modeling versus the torque measured using a commercial torque sensor (sudden load change).
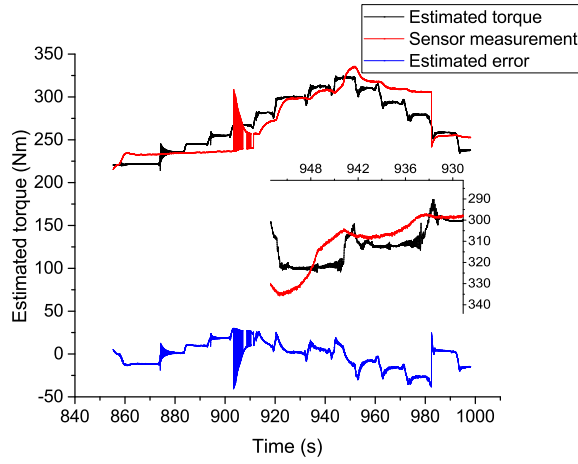
on modeling and using a commercial torque sensor is shown in Fig. 9, Fig. 10, Fig. 11 and Fig. 12, respectively. The estimated error is the difference between the estimated torque and the sensor measurement. It is evident that in the process of a slow change of the load torque, the maximum difference between the evaluated torque due to the proposed method and the measured torque obtained using the commercial sensor is 84.8 Nm, and its RMS value is 42.3 Nm. In the process of rapid change of the torque, these two values are 400 Nm and 67.06 Nm, respectively. Similarly, in the process of a sudden load change and a step-by-step load change, these indices are 80.23 Nm, 32.99 Nm, 29.9 Nm, and 14.48 Nm, respectively.

It is evident that the error of the torque estimation method, based on the improved harmonic compliance model, is less than 84.8 Nm when the load torque changes slowly. However, the error increases when the load torque changes rapidly. The difference between the estimated value and the measured value is mainly caused by the dimensional limitation of the fitting functions and the un-modeled friction of the robotic joint. By increasing the dimensions of polynomials and the Fourier series, the error can be reduced to some extent. The main advantage of this method is that the programming progress is simple, and the computational burden is small. Thus, it has good real-time performance. Therefore, it is more suitable for the application scenarios where the load torque changes slowly and the required accuracy is not very high, but the real-time measurement is critical.

A comparison of the estimated results using the torque estimation method based on the BP neural network and using the commercial torque sensor is shown in Fig. 13, Fig. 14,

Fig. 12.   Estimated torque based on modeling versus the torque measured using a commercial torque sensor (static load change).

Fig. 14.   Estimated torque based on the BP neural network versus the torque measured using a commercial torque sensor (fast load change).
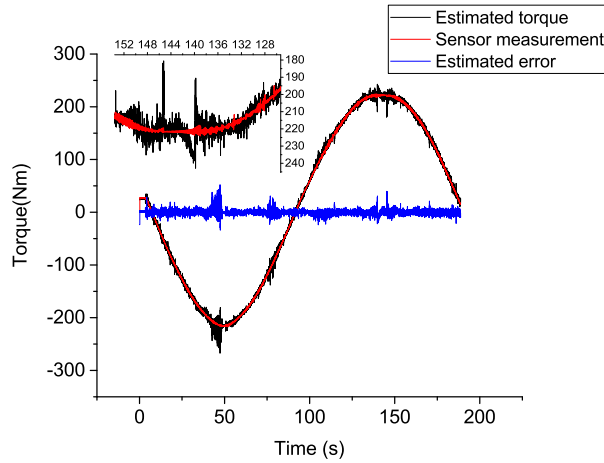

Fig. 13.   Estimated torque based on the BP neural network versus the torque measured using a commercial torque sensor (slow load change).

Fig. 15.   Estimated torque based on the BP neural network versus the torque measured using a commercial torque sensor (sudden load change).

Fig. 15 and Fig. 16, respectively. It is evident from these figures that in the process of slow change of the load torque, the maximum difference between the estimated torque due to the proposed method (based on the BP neural network and the measurements performed using a commercial torque sensor) is 29.9 Nm with an RMS value of 14.48 Nm. In the case of a rapid change of the torque, these two indices are 167.1 Nm and 11.3 Nm. Similarly, in the process of sudden load change and a step-by-step load change, these values are 43.1 Nm, 2.84 Nm, 20.4 Nm, and 5.9 Nm.

To analyze the performance of these two proposed torque estimation methods more effectively, we calculate an index called the error rate. This index is the ratio of the estimated error of each method to the rated torque of the experimental harmonic reducer, and they are compared as shown in Fig. 17. It is evident that the error of the torque estimation method (based on the BP neural network) is very small for all the load change situations. Therefore, this method is suitable for applications that require high measurement accuracy, or for cases in which the external load changes rapidly and irregu-
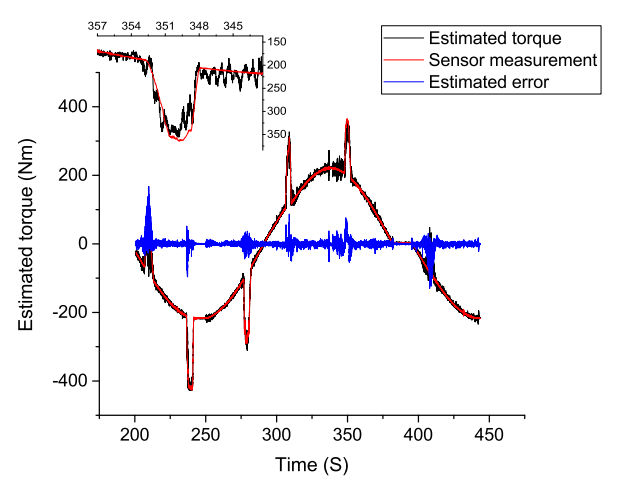

Fig. 16.   Estimated torque based on the BP neural network versus the torque measured using a commercial torque sensor (static load change).
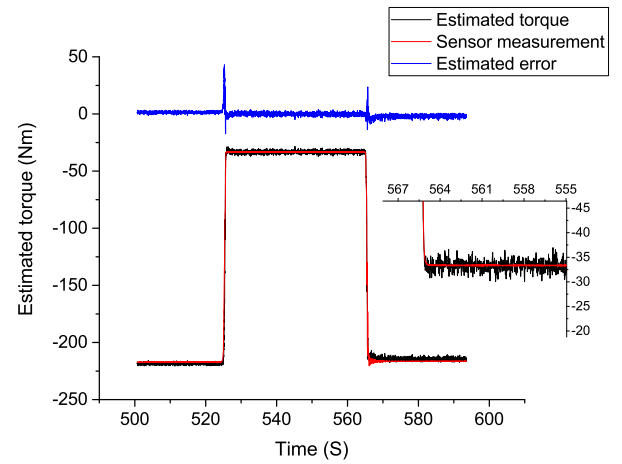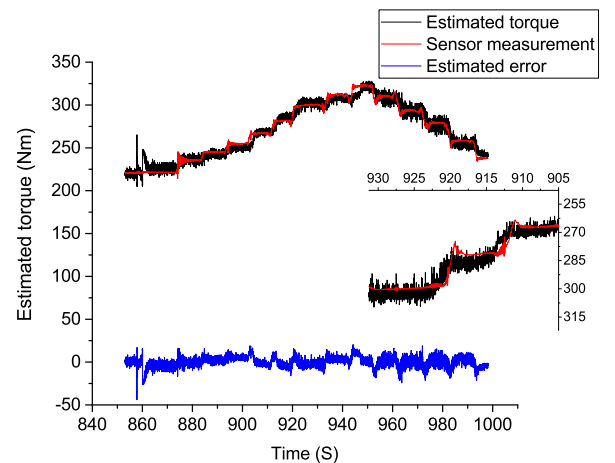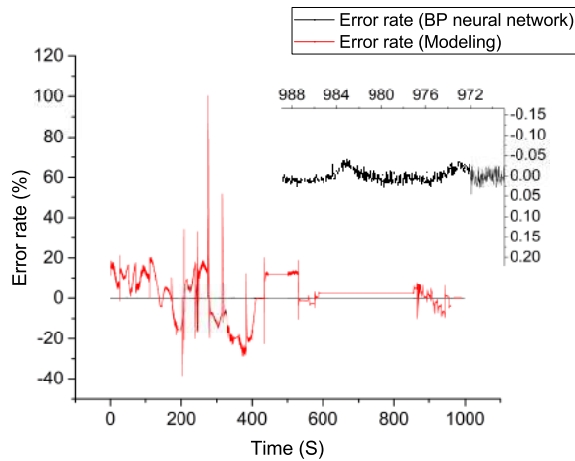
Fig. 17. Error rate comparison for the two proposed methods.

larly. However, compared with the method based on modeling, the programming progress is complex, and the computational burden is significant, which leads to its relatively poor real-time performance.

V. CONCLUSION

In this paper, two novel methods were proposed to estimate the output torque of a robotic joint with a harmonic reducer based on deformation calibration. According to the experimental results, both methods have sufficient measurement accuracy and are applicable to different scenarios depending on their specific performance and principle. In addition, they avoid the problems of increasing joint flexibility and excessive joint size that arise from the installation of commercial torque sensors. Moreover, neither of them require a change of the original structure of the existing robotic joint. In addition, the encoder installed at the output-side of the harmonic reducer can also be used to measure the accurate joint output angular position, which can potentially increase the position control precision of the robot. The results obtained may have application prospects with regards to robotic hybrid position/force control.

REFERENCES

[1] Karen Lohmann Siegel, Thomas M Kepple, and Steven J Stanhope. Joint moment control of mechanical energy flow during normal gait . *Gait and Posture*, 19(1):69–75, 2004.

[2] Daniel Brown and Mason Peck. Energetics of control moment gyroscopes as joint actuators. *Journal of Guidance Control and Dynamics*, 32(6):1871–1883, 2009.

[3] L. Yang, Z. Liu, and Y. Zhang. Adaptive fuzzy yaw moment control of humanoid robot based on ankle joint. In *Control Conference*, 2015.

[4] Minoru Hashimoto, Toshiaki Shimono, Ken Ichi Koreyeda, Hideho Tanaka, Y Koyosawa, and Hideki Hirabayashi. Experimental study on torque control using harmonic drive built-in torque sensors anddagger;. *Journal of Field Robotics*, 15(8):435–445, 2015.

[5] Niu Feng, Bingsen Wang, Andrew S. Babel, Kui Li, and Elias G. Strangas. Comparative evaluation of direct torque control strategies for permanent magnet synchronous machines. *IEEE Transactions on Power Electronics*, 31(2):1408–1424, 2015.

[6] Zhaopeng Chen, Neal Y. Lii, Minghe Jin, Shaowei Fan, and Liu Hong. Cartesian impedance control on five-finger dexterous robot hand dlr-hit ii with flexible joint. In *International Conference*, 2010.

[7] Wei He, Yiting Dong, and Changyin Sun. Adaptive neural impedance control of a robotic manipulator with input saturation. *IEEE Transactions on Systems Man Cybernetics Systems*, 46(3):334–344, 2017.

[8] Haifa Mehdi. Stiffness and impedance control using lyapunov theory for robot-aided rehabilitation. *International Journal of Social Robotics*, 4(1 Supplement):107–119, 2012.

[9] Guo Jin, Maoxun Li, Ho Pei, and Hongliang Ren. Design and performance evaluation of a force/torque sensor for tele-operated catheterization procedures. *IEEE Sensors Journal*, 16(9):3208–3215, 2016.

[10] Yanzhi Zhao, Caifeng Zhang, Dan Zhang, Zhongpan Shi, and Tieshi Zhao. Mathematical model and calibration experiment of a large measurement range flexible joints 6-upr six-axis force sensor. *Sensors*, 16(8):1271, 2016.

[11] Marco Randazzo, Matteo Fumagalli, Francesco Nori, Lorenzo Natale, Giorgio Metta, and Giulio Sandini. A comparison between joint level torque sensing and proximal f/t sensor torque estimation: Implementation on the icub. In *IEEE/RSJ International Conference on Intelligent Robots and Systems*, 2011.

[12] D. Helmick, A. Okon, and M. Dicicco. A comparison of force sensing techniques for planetary manipulation. In *IEEE Aerospace Conference*, 2006.

[13] Julio Gonzalo Garcia, Anders Robertsson, Juan Gmez Ortega, and Rolf Johansson. Sensor fusion for compliant robot motion control. *IEEE Transactions on Robotics*, 24(2):430–441, 2008.

[14] Chi Ting Yeh, Nan Chyuan Tsai, Hsin Lin Chiu, and Chung Yang Sue. Digital high-resolution torque sensor and signal processing. *IEEE Sensors Journal*, 15(4):2093–2100, 2015.

[15] Sarmad Shams, Yeong Lee Ji, and Changsoo Han. Compact and lightweight optical torque sensor for robots with increased range. *Sensors and Actuators A Physical*, 173(1):81–89, 2012.

[16] Sarmad Shams, Dongik Shin, Jung Soo Han, Yeong Lee Ji, Kyoosik Shin, and Chang Soo Han. Compact design of a torque sensor using optical technique and its fabrication for wearable and quadruped robots. In *IEEE/RSJ International Conference on Intelligent Robots and Systems*, 2011.

[17] Tomohiro Kawakami, Ko Ayusawa, Hiroshi Kaminaga, and Yoshihiko Nakamura. High-fidelity joint drive system by torque feedback control using high precision linear encoder. In *IEEE International Conference on Robotics and Automation*, 2010.

[18] Minoru Hashimoto, Yoshihide Kiyosawa, and Richard P. Paul. A torque sensing technique for robots with harmonic drives. *Robotics and Automation IEEE Transactions on*, 9(1):108–116, 1993.

[19] H. D. Taghirad and P. R. Belanger. Intelligent built-in torque sensor for harmonic drive systems. *IEEE Transactions on Instrumentation and Measurement*, 48(6):1201–1207, 2002.

[20] P. R. Belanger and H. D. Taghirad. Torque ripple and misalignment torque compensation for the built-in torque sensor of harmonic drive systems. *IEEE Transactions on Instrumentation and Measurement*, 47(1):309–315, 1998.

[21] In Moon Kim, Hwi Su Kim, and Jae Bok Song. Design of joint torque sensor with reduced torque ripple for a robot manipulator. *International Journal of Precision Engineering and Manufacturing*, 13(10):1773–1779, 2012.

[22] In Moon Kim, Hwi Su Kim, and Jae Bok Song. *Embedded Joint Torque Sensor with Reduced Torque Ripple of Harmonic Drive*. 2013.

[23] Byung Jin Jung, Byoung Chul, Seonggi Kim, Jachoon Koo, and Hyung-pil Moon. Torque ripple compensation method for joint torque sensor embedded in harmonic drive using order analysis. In *Sensors*, 2014.

[24] Byung Jin Jung, Byungchul Kim, Hyouk Ryeol Choi, Ja Choon Koo, and Hyungpil Moon. Joint torque sensor embedded in harmonic drive using order tracking method for robotic application. *IEEE/ASME Transactions on Mechatronics*, PP(99):1–1, 2017.

[25] Zhi Hao Xu, Sheng Ching Wang, Tsung Shune Chin, Jen Yuan Chang, and Cheng Kuo Sung. Multi-pole fine magnetic scale for high-resolution magnetic encoders evidenced by a simplified method. *Microsystem Technologies*, 20(8-9):1491–1496, 2014.

[26] Lei Wang, Yongde Zhang, Shuanghui Hao, Baoyu Song, Minghui Hao, and Zili Tang. Study on high precision magnetic encoder based on pmsm sensorless control. *Sensor Review*, 36(3):267–276, 2016.

[27] Hongwei Zhang, Saleh Ahmad, and Guangjun Liu. Torque estimation technique of robotic joint with harmonic drive transmission. In *IEEE International Conference on Robotics and Automation*, 2013.

[28] Hongwei Zhang, Saleh Ahmad, and Guangjun Liu. Torque estimation for robotic joint with harmonic drive transmission based on position measurements. *IEEE Transactions on Robotics*, 31(2):322–330, 2017.

[29] Zhiguo Shi and Guangjun Liu. Torque estimation of robot joint with harmonic drive transmission using a redundant adaptive robust extended

kalman filter. In *IEEE International Conference on Robotics and Automation*, 2014.

[30] Zhiguo Shi, Yuankai Li, and Guangjun Liu. Adaptive torque estimation of robot joint with harmonic drive transmission. *Mechanical Systems and Signal Processing*, 96:1–15, 2017.

[31] Curt Preissner, Thomas J Royston, and Deming Shu. A high-fidelity harmonic drive model. *Journal of Dynamic Systems, Measurement, and Control*, 134(1):011002, 2012.

[32] C. W. Kennedy and J. P. Desai. Modeling and control of the mitsubishi pa-10 robot arm harmonic drive system. *IEEE/ASME Transactions on Mechatronics*, 10(3):263–274, 2005.

[33] H.drive technologies. (2012) ultra-flat component sets and gearheads. [online]. *Available:http://www.harmonicdrive.net/support/catalogs/*.

[34] Fathi H Ghorbel, Prasanna S Gandhi, and Friedhelm Alpeter. On the kinematic error in harmonic drive gears. *Journal of Mechanical Design*, 123(1):90–97, 2001.

[35] Edwin K. P. Chong and Stanislaw H. Zak. *An Introduction to Optimization, 4th Edition*. 1996.

[36] Gene H. Golub and Charles F. Van Loan. Matrix computations, 3rd ed. 1996.

[37] Sebastian Thrun. *Probabilistic robotics*. 2005.

[38] B. H. M. Sadeghi. A bp-neural network predictor model for plastic injection molding process. *Journal of Materials Processing Technology*, 103(3):411–416, 2000.

[39] Joshua Alspector, Ronny Meir, B. Yuhas, A. Jayakumar, and D. Lippe. A parallel gradient descent method for learning in analog vlsi neural networks. In *Advances in Neural Information Processing Systems*, 1992.

Fengfeng(Jeff) Xi received the B.Eng. and M.Sc. degree from Shanghai University, ShangHai, China, in 1982 and 1984, respectively, and the Ph.D. degree from the University of Toronto, Toronto, Canada, in 1993. He is currently a Professor in the Department of Aerospace Engineering Ryerson University, Toronto, Canada. His current research interests include sensor responsive design with application to smart aircraft cabins and aircraft manufacturing automation including robotic fastening/polishing/deburring/inspection.

Dunyi Zhou received the B.Eng. degree in engineering from Northeast Forestry University, Harbin, China, in 2018. He is currently pursuing the M.Eng. degree in mechanical engineering from Harbin Institute of Technology (Shenzhen), Shenzhen, China. His research interests include machine vision, path programming, and cooperative robot.

Bing Li received the B.Eng. and M.Eng. degrees in engineering from Liaoning Technical University, FuXin, China, in 1996 and 1999, respectively, and the Ph.D. degree from the Hong Kong Polytechnic University, Hong Kong, China, in 2001. He is currently a Professor at the Research Institute of Aerospace Equipment and Intelligent Manufacturing, Department of Harbin Institute of Technology (Shenzhen), Shenzhen, China. His current research interests include robotics, bionic robot, space agency, and mechanical vibration and control.

Yanshu Song received the B.Eng. degree in engineering from Harbin Institute of Technology, Harbin, China, in 2017. He is currently pursuing the M.E. degree in mechanical engineering from Harbin Institute of Technology (Shenzhen), Shenzhen, China. His research interests include machine vision, path programming, and machine learning.

Hailin Huang received his B.Sc. degree in Mechanical Design and Automation from Harbin Institute of Technology, Harbin, China, in 2005, and M.Sc. and Ph.D. degrees in Mechatronics Engineering from Harbin Institute of Technology Shenzhen Graduate School, Shenzhen, China, in 2007 and 2012, respectively. From January 2012 to June 2012, he was a Research Associate in the Department of Mechanical and Aerospace Engineering, Nanyang Technological University, Singapore. From November 2012 to Judy 2014, he was a Postdoctoral Fellow in the Department of Mechanical and Biomedical Engineering, City University of Hong Kong. In July 2014, he joined Harbin Institute of Technology Shenzhen Graduate School, Shenzhen, China. He is currently an assistant professor at Harbin Institute of Technology, Shenzhen. His research interests include robotic mechanism and motion control.

Fei Liu received the B.Eng. and M.Eng. degrees in engineering from Yangtze University, Jingzhou, China, in 2005 and 2008, respectively. He is currently pursuing the Ph.D. degree in mechanical engineering from Harbin Institute of Technology(Shenzhen), Shenzhen, China. His research interests include parallel robots and manipulator.